Post-deposition annealing effects of copper oxide (Cu_2O) thin film deposited using E-beam evaporation

Salam Surjit Singh[1], Biraj Shougaijam[2], Mir Waqas Alam[3], and Naorem Khelchand Singh[1,*]

[1] *Department of Electronics and Communication Engineering, National Institute of Technology Nagaland, Dimapur, Nagaland 797103, India*
[2] *Department of Electronics and Communication Engineering, Manipur Technical University, Takyelpat, Imphal, Manipur 795004, India*
[3] *Department of Physics, College of Science, King Faisal University, 31982 Al-Ahsa, Saudi Arabia*

Received: 17 January 2023
Accepted: 19 March 2023
Published online: 30 March 2023

© The Author(s), under exclusive licence to Springer Science+Business Media, LLC, part of Springer Nature 2023

ABSTRACT

In this work, a thin copper (I) oxide (Cu_2O) layer was deposited on p-type silicon substrates using the E-beam evaporation method without using any catalyst. The fabricated copper oxide sample was annealed at different annealing temperatures ranging from 300 to 700 °C. X-ray diffraction (XRD) and scanning electron microscopy (SEM) were used to examine the structural and morphological analysis of the as-deposited and annealed samples. The XRD results reveal the phase transition of the copper (II) oxide (CuO) sample and the presence of CuO was also confirmed by peaks at $\sim$ 35.79° and $\sim$ 38.94°, which correspond to (11 − 1) and (220) crystal planes, respectively. A semi-cubic-shaped rough surface was observed from the top view SEM image after annealing at 600 °C for 1 h. Also, surface composition was evaluated by the X-ray photoelectron spectroscopy which strongly indicates the formation of Cu_2O in the as-deposited sample, which changes to the CuO phase after annealing at 600 °C. Further, the absorbance spectra show absorption enhancement in the IR region after annealing of the Cu_2O thin films . Moreover, it was found that the optical bandgap of the as-deposited sample decreases from $\sim$ 2.17 to $\sim$ 1.43 eV after annealing. Therefore, this process of developing high quality copper oxide-TF deposited on Si substrate using the E-beam evaporation technique can be used to develop a variety of opto-electronic applications.

Address correspondence to E-mail: khelchand.singh@gmail.com

https://doi.org/10.1007/s10854-023-10283-3

1 Introduction

Over the past few years, metal oxide semiconductors have been extensively used due to their favorable optical, electrical and magnetic properties for electronic applications such as photodetectors [1], non-volatile memory [2], solar cells [3], photocatalysts [4], microwave absorption [5, 6], gas sensors [7] and DSSCs [8]. Among the oxide materials, copper oxide has caught the attention of many researchers owing to its potential application in optoelectronic devices as it has strong corrosive resistance as compared to other metal oxides. Copper oxide has shown good electrical properties, low-cost production, good stability, non-toxic and high optical absorption in the visible as well as near infrared regions [9]. Copper oxide is a native p-type semiconductor that can be found in two forms depending on the deposition techniques: cupric oxide (CuO) with a bandgap of $\sim$ 1.2 - 1.9 eV and a monoclinic crystal structure (a = 4.688 Å, b = 3.4229 Å, c = 5.131 Å and β = 99.51°) and cuprous oxide (Cu_2O) with a bandgap of $\sim$ 2.0 - 2.5 eV and cubic structure (a = 4.27 Å). It has a high absorption co-efficient of $\sim 10^5$ cm^{-1} at 300 K, good thermal conductivity of $\sim$ 76.5 Wm^{-1} K^{-1}. Also, it can have a good electrical resistance of 10–10^5 ohms/cm depending on the method of fabrication [10]. Because of these properties, copper oxide has been widely used in various applications such as super capacitors [11], photovoltaics [12], glucose sensors [13], lithium-ion batteries [14], water splitting [15], H_2S sensing [16], biomaterials [17] and catalysts [18]. However, the electrical properties of the material are mainly influenced by the defects, grain boundaries, surface adsorbed oxygen and specific surface areas [19]. It is well known that metal oxide nanostructure film contains a number of point defects and surface defects, that have deviated from their original stoichiometry. With the advancement in material science and engineering, the structural, optical and electrical properties of a material can be controlled by varying the method of deposition used and the post-annealing treatment. Several methods of chemical and physical manufacturing methods, such as sol–gel [20], chemical vapor deposition [21], electrodeposition [22], hydrothermal [23], reactive sputtering [24] and molecular beam epitaxy [25] have been employed for the preparation of copper oxide-TF. Prabu et al. reported that copper oxide-TF were deposited on glass substrates by spray pyrolysis techniques and studied the various key properties of the films after annealing at different temperatures [26]. Again, Abinaya et al. reported that p-type copper oxide-TF is deposited on a silica glass substrate by DC magnetron sputtering. A pure copper metal target is used as the source material for the deposition of copper oxide film, followed by annealing at various atmospheric conditions to study various electrical and structural properties of the film [27]. But very few reports were available on the fabrication of copper oxide film over silicon substrates using E-beam evaporation techniques. E-beam is a versatile technique that can be used to deposit uniform TF metal-oxide over the substrate [28]. It is also useful for depositing high melting point material in economical and simple techniques for manufacturing TF. The properties of the E-beam deposited film mainly depend on parameters such as accelerating voltage, substrate temperature, distance from target to source, ambient pressure inside the E-beam chamber, thickness etc. [29]. However, most of the metal oxide films formed by E-beam evaporation techniques generate oxygen vacancies and surface deformation, which can be reduced by heat treatment during the deposition. Again, post-deposition heat treatments might be one useful way to control and improve the microstructural, optical and electrical properties of films [30]. Therefore, annealing at an optimal temperature will reduce structural defects, which reduce oxygen vacancies and improve the crystal quality of the metal oxide film.

In this work, an attempt has been made to prepare a copper oxide-TF using the E-beam evaporation technique on a p-type silicon substrate without the use of a catalyst. Also, post-deposition annealing is carried out using muffle furnace. The effect of the annealing temperature on the structural, morphological and optical characteristics of the film was investigated. The structural properties of the sample at different annealing temperatures are determined using X-ray diffraction (XRD). The morphological structure of the fabricated sample is also analysed using scanning electron microscopy (SEM) and energy dispersive X-ray spectroscopy (EDX). Again, the optical properties of the sample are analysed using UV–Vis spectroscopy. Here, we are trying to study the effect of annealing on the crystal quality of the film in terms of the structural, morphological and optical properties of the copper oxide-TF. Thus, the present work will give new visions in the field of

optoelectronic devices by improving the crystallinity of the copper oxide film after annealing at an optimum temperature.

2 Experimental details

Copper oxide-TF was deposited on 1 × 1 cm silicon wafers (resistivity ~ 2 ohms/cm^2) using electron beam evaporation inside the vacuum chamber (Model No.: Smart Coat 3.0). Initially, the silicon substrate was properly cleaned by submerging it for 2 min each in acetone, methanol and DI water. Furthermore, the clean Si substrate was placed on the substrate holder and put inside the vacuum chamber, in which the substrate holder was placed inclined vertically with respect to the source material. The copper oxide source material was loaded on to the graphite crucible and the chamber was evacuated with the help of a rotary pump and further with a diffusion pump to maintain a base pressure of 5×10^{-6} mbar. The chamber pressure lowers to 9×10^{-5} mbar during the deposition process, which may be caused by the release of oxygen from the source material. In this experiment, the rate of deposition is controlled and tracked using digital thickness monitoring (DTM), which is maintained at a rate of ~ 0.4 Å sec^{-1}. The source material used for deposition is Cu_2O (99.9999% pure) and p-type silicon substrate (111) from MTI (KJ Group) as a substrate. The XRD measurements were executed by the PANalytical X'Pert Pro diffractometer under Cu K-alpha radiation (k = 1.54060 Å) at 30 mA and 40 kV to determine the crystal structure and phase transformation of copper oxide-TF. To examine the structural and surface morphological properties of copper oxide-TF, SEM (Carl Zeiss Sigma 3000) integrated with EDX was used. The optical properties of both the as-deposited and annealed samples were measured using a UV-Vis spectrometer (Hitachi UH4150). The composition and chemical state of different elements present in the films were determined using X-ray photoelectron spectroscopy (Model No. PHI5000 Versa Probe III).

3 Results and discussion

3.1 Structural properties Analysis

The as-deposited Cu_2O-TF is annealed at various temperatures between 300 to 700 °C and characterized using XRD. The diffraction patterns of the copper oxide-TF samples are shown in Fig. 1. As seen in Fig. 1a, the diffraction peak of the as-deposited copper oxide-TF is observed at ~ 42.66° corresponding to (200) of copper (I) oxide (cuprous) crystal phase [JCPDS Card No. 005-0667]. This as-deposited sample exhibits lower diffraction peak intensities, which is attributed to the formation of more oxygen vacancies [31]. A more intense peak appears at ~ 35.79° and ~ 38.94° after annealing at 300 °C, which is assigned to (1 − 11) and (200) of the copper (II) oxide (cupric) crystal plane, respectively, as shown in Fig. 1b [JCPDS card No. 048-1548]. This Cu_2O phase start changing it phase from Cu_2O to CuO at an annealing temperature of around 300 °C is due to an increase in lattice oscillations and molecular vibrations. As a result, the weak interconnection bonds between the Cu and O atoms are broken, resulting in a phase transformation to the CuO crystal structure. This causes a change in the bonding properties and ionic patterns of the crystal structures. At this temperature, several copper atoms ionized from Cu^{1+} to Cu^{2+} by losing one electron. Additionally, the half-fill orbital in the copper atom's outermost 3d valence shell (…$3p^6 3d^9$), which is more excited to participate in the process, makes the copper atom in the Cu^{2+}

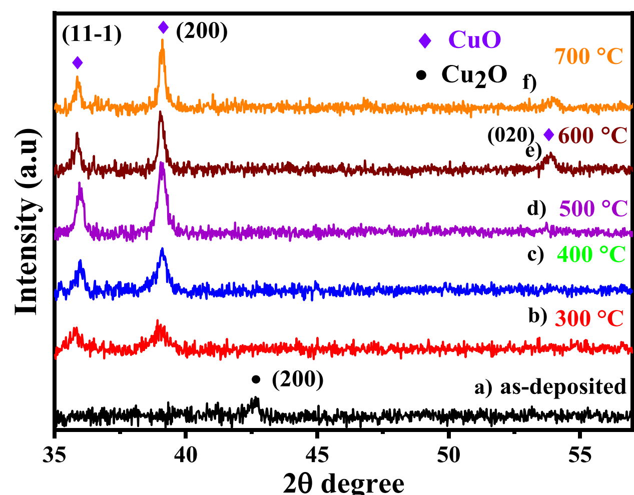

Fig. 1 XRD results of copper oxide-TF annealed at various temperatures

ionization state more unstable than the atoms in Cu^{1+} [32]. Nair et al. reported that TF deposited using chemical processes form cuprite oxide (Cu_2O) structures, which convert to cupric oxide (CuO) after annealing the sample at 350 °C in air [33]. Again, Raghavendra et al. also reported that there is a change in the copper oxide phase from Cu to CuO, which proves that the CuO phase transition temperature occurs at 300 °C [34, 35].

Moreover, with the increase in the heating temperature from 300 to 500 °C, the peak intensity of the diffracted peaks at ~ 35.79° and ~ 38.94° increases without changing the peak orientation, which is shown in Fig. 1c and d. Further, as the annealing temperature increases from 500 to 700 °C, the sample shows an extra peak at ~ 53.85 °, which is indexed to the (020) crystal of the CuO, apart from the previous peaks observed at the previous lower annealing temperature [JCPDS Card No. 048-1548]. It is also observed that no peak shift or formation of the Cu_2O phase was found with an increase in the annealing temperature of the sample. No matter how stable the CuO is, tenorite CuO structures will form due to the rising molecular vibrations and lattice oscillations in the air atmosphere according to the $2\,Cu_2O + O_2 \rightarrow 4\,CuO$ equation [32]. This shows that the crystallinity of CuO-TF improves with an increase in the annealing temperatures, which may also be due to the filling up of oxygen vacancies during the process [36, 37]. Also, high temperatures reduce the symmetry, but they also shape copper atoms with excellent electrical stability. Again, using Scherrer's equation, the average crystallite size (D) values for the as-deposited and annealed samples are determined from the XRD graph in Fig. 1 [38].

$$D = \frac{k\lambda}{\beta\cos\theta} \quad (1)$$

where $k = 0.9$, θ is the Bragg angle, $\lambda = 1.54$ Å and β is the full width half maximum (FWHM), which is expressed in radians. The calculated average crystallite size value from Scherrer's equation as a function of annealing temperature is presented in Table 1.

When the Cu_2O dominated as-deposited film is annealed at 300 °C, the calculated average crystallite size of the sample is ~ 15.77 nm, which is larger than that of the as-deposited Cu_2O-TF, i.e., ~ 12.98 nm. As the annealing temperature increases from 300 to 600 °C, the average crystallite size gradually increases from ~ 15.77 to ~ 33.54 nm. This shows a higher rate of crystal growth for CuO samples, which also improves the mobility of the atoms by acquiring adequate kinetic energy to travel freely on the atomic surface of the CuO. Moreover, as the annealing temperature increases, the thermal energy increases, leading to the migration of atoms and particles that get agglomerated, forming the larger grains [39]. In addition, morphological structure of the sample and variation in grain growth is also observed from the SEM images, which will be explained in the later section.

It is clearly shown in Fig. 2 that the average crystallite size of the as-deposited sample increases with an increase in the annealing temperature and also the variation in the lattice strain with respect to the annealing temperature. From the thermodynamic perspective, the oxidation process of Cu_2O to CuO occurs depending on the time of reaction and the temperature [40]. It is not worthy to mention that the crystallinity of the CuO is improved, with increasing annealing temperatures, thereby reducing the amount of lattice imperfections (defects and grain boundaries) in the crystal structure [34]. However, a further rise in the annealing temperature to 700 °C leads to breaking of the CuO bond, which opposed the atom from moving freely, resulting in defects and stress in CuO-TF, thereby reducing the average grain size of the crystal, as shown in Fig. 2. Similarly, Pandey et al. reported that RF sputtered deposited ZnO-TF show breaking of ZnO bonds after post annealing at temperature higher than 700 °C [41]. Moreover, the dislocation density, i.e., the length of the dislocation lines per unit crystal volume and the micro-strain of the as-deposited and annealed samples were also calculated using the equation.

$$\delta = \frac{1}{D^2} \quad (2)$$

$$\epsilon = \frac{\beta\cos\theta}{4} \quad (3)$$

where, D is the crystallite size and β is the FWHM, which is calculated from the XRD peak. It is observed from Table 1 that the dislocation density and the lattice strain were reduced from $\sim 4.021 \times 10^{15}$ (lines/m^2) to $\sim 0.889 \times 10^{15}$ (lines/m^2) and ~ 0.0705% to ~ 0.0346%, respectively, when the annealing temperature was increased from 300 to 600 °C. This decreased lattice strain parameter is due to reduction in point defects (or an improvement in the

Table 1 Lattice strain, dislocation density and average crystallite size with reference to annealing temperature

Serial no.	Temperature (°C)	D (nm)	Strain (%)	Dislocation density (δ) × 10^{15} (lines/m^2)
1.	As-deposited	12.98	0.0718	5.937
3.	300 °C	15.77	0.0705	4.021
4.	400 °C	20.55	0.0536	2.368
5.	500 °C	24.54	0.0448	1.694
6.	600 °C	33.54	0.0346	0.889
7.	700 °C	33.03	0.0347	0.916

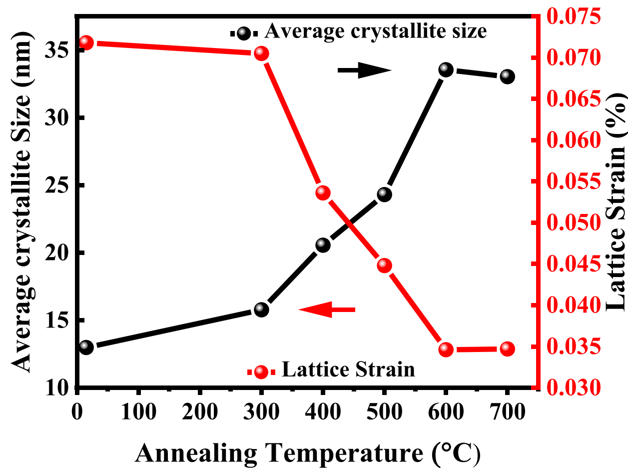

Fig. 2 Crystal size and lattice strain with respect to annealing temperatures

lattice defects) along the grain boundaries as the average crystallite size increases with the increase in annealing temperature [42]. However, the average crystallite size of the CuO-TF reduces to ~ 33.03 nm while increasing the annealing temperature to 700 °C, which also increases the lattice strain and dislocation density to ~ 0.0347% and ~ 0.916 × 10^{15} (lines/m^2), respectively.

Therefore, it can be concluded from this XRD analysis that the micro-strain and dislocation density increase as the annealing temperature is increased beyond 600 °C. As a result, the crystallite grain size of the sample decreases. Therefore, annealing a copper oxide sample at 600 °C is the optimal temperature for producing good-quality crystallite film, which can be applicable in designing optoelectronic devices.

3.2 Optical analysis

The optical characteristics of copper oxide-TF sample at different annealing temperatures were analyzed using a UV–Vis–NIR spectrophotometer in the wavelength range of ~ 400 nm to ~ 1000 nm. The absorption spectra of the as-deposited and annealed fabricated samples are shown in Fig. 3. It is observed that the as-deposited copper oxide sample, shows multiple humps at ~ 550 nm and ~ 700 nm, which may be due to high defect density near the band edge. As the annealing temperature increases, the CuO film exhibits sharp absorption at around ~ 750 nm and shifts toward the more IR region, which may be attributed to good crystallinity and a low defect concentration in the film. The bandgap energies of the as-deposited and annealed copper oxide film are extracted from the Tauc plot by extrapolating the linear part of the graph, which is shown in Fig. 3b. The calculated bandgap of the as-deposited copper oxide sample is found to be ~ 2.17 eV. As the copper oxide sample is annealed at 300 °C the Cu_2O crystal plane, which is observed in the as-deposited sample, transforms into a CuO crystal plane. As a result, the bandgap of the annealed sample also decreases. This result shows that an increase in the thermal annealing temperature reduces the bandgap energies of the copper oxide sample [43]. Similarly, Radu et al. reported that the bandgap energies of the copper oxide-TF reduced as the annealing temperature increased. Further, crystal phase transformation from Cu_2O to CuO is also obtained by controlling the annealing time and temperature [44]. Furthermore, as the annealing temperature increases from 300 to 600 °C, the bandgap of copper oxide decreases from ~ 1.89 to ~ 1.43 eV. According to Hojabri et al., the crystal quality of Cu film improves after annealing at 450 °C. As a result, the optical bandgap decreases with an increase in the annealing temperature of the film [45].

However, when the annealing temperature is increased to 700 °C, the bandgap of the sample slightly increases to ~ 1.48 eV, which is shown in

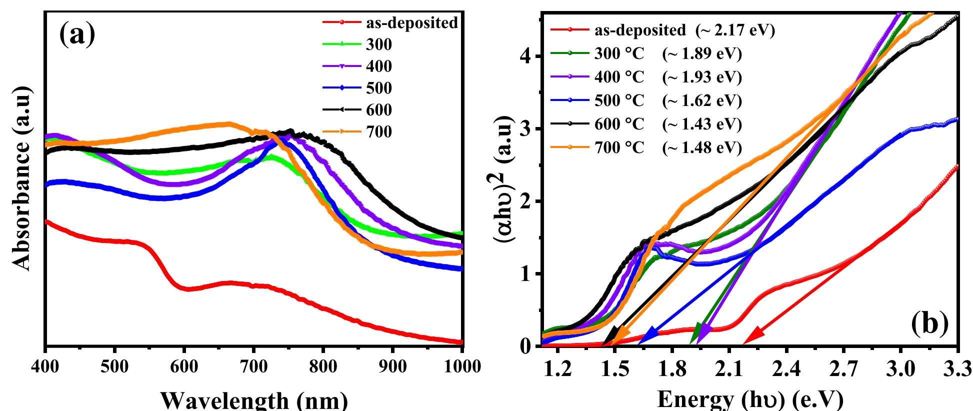

Fig. 3 **a** UV–Vis absorption spectra of as-deposited and annealed samples and **b** Tauc plots of as-deposited and annealed copper oxide samples

Fig. 3b. In addition, the absorption spectra of the copper oxide TF sample annealed at 600 °C are more shifted to the IR region as compared to other annealed samples. The increase in the absorption may be due to improved crystallinity and larger grain size after annealing which, thereby reducing the band gap and enhance the absorption in the IR region [46]. Also, it is well observed from the Tauc plot graph in Fig. 3b that the bandgap energies of the copper oxide film annealed at 600 °C show much lower bandgap energies as compared to the other annealed samples. It is evident from these absorption spectra that the overall absorption intensity of the annealed CuO-TF sample increases in the IR region, which may have potential for developing IR light detectors and other optoelectronic devices. Based on the XRD and absorption analysis, it was observed that the CuO sample annealed at 600 °C exhibited a higher degree of crystallinity and enhanced absorption in the infrared region. Therefore, the as-deposited Cu_2O-TF and CuO-TF samples annealed at 600 °C have been chosen for further investigation.

3.3 Surface morphology analysis

Figure 4a shows the SEM images of the as-deposited Cu_2O-TF. These images clearly reveal that a compact and crack-free copper oxide-TF has been successfully deposited uniformly on the Si substrate. It is also observed from the top-view image shown in the inset of Fig. 4a that well-defined grains have a spherical shape and a uniform distribution on the Si substrate, with an average grain size of $\sim$ 16.73 nm. Further, as seen from the cross-sectional image of Fig. 4b, the thickness of the copper oxide-TF is determined to be $\sim$ 100 nm. In comparison to the calculated values from the XRD data, the average grain size of the as-deposited sample as seen in SEM is larger. This is due to the fact that the average grain size in SEM analysis is determined by the spacings between the visible grain boundaries, but the Scherrer relation from XRD analysis provides the size of the crystalline domain that coherently diffracts from the X-rays [31].

Figure 4c and d display the top-view and cross-section SEM images of the copper oxide film that was formed after being annealed at 600 °C. It is observed that the semi-spherical shapes seen from the top view SEM image of the as-deposited copper oxide-TF change to a hard packing structure with a semi-cubic shape after annealing at 600 °C, as shown in Fig. 4c [47]. The calculated average grain size of the annealed (600 °C) CuO-TF sample is found to $\sim$ 64.54 nm, which is observed in Fig. 4c inset. Also, the more rough nature of the film is observed from the cross-sectional image of the annealed sample, which is shown in Fig. 4d. As the annealing temperature increases, the isolated atoms get diffused, increasing the grain size of the sample and creating irregular grain shapes [48]. Furthermore, the elemental identification and composition analysis, i.e., EDX is conducted on both the as-deposited and annealed films. And, the corresponding EDX spectra of the sample is shown in Fig. 5a and b. From this EDX analysis, it is clearly confirmed that copper (Cu), oxygen (O) and silicon (Si) are present for both the as-deposited and annealed copper oxide samples. The percentage content of oxygen in the annealed sample is $\sim$ 14%, which is more than the as-deposited sample, which contains only 1.7%. This increase in the oxygen concentration of the annealed sample clearly indicates that the oxygen vacancy present in the as-deposited sample reduces with an increase in the annealing temperature of the film. Therefore, this

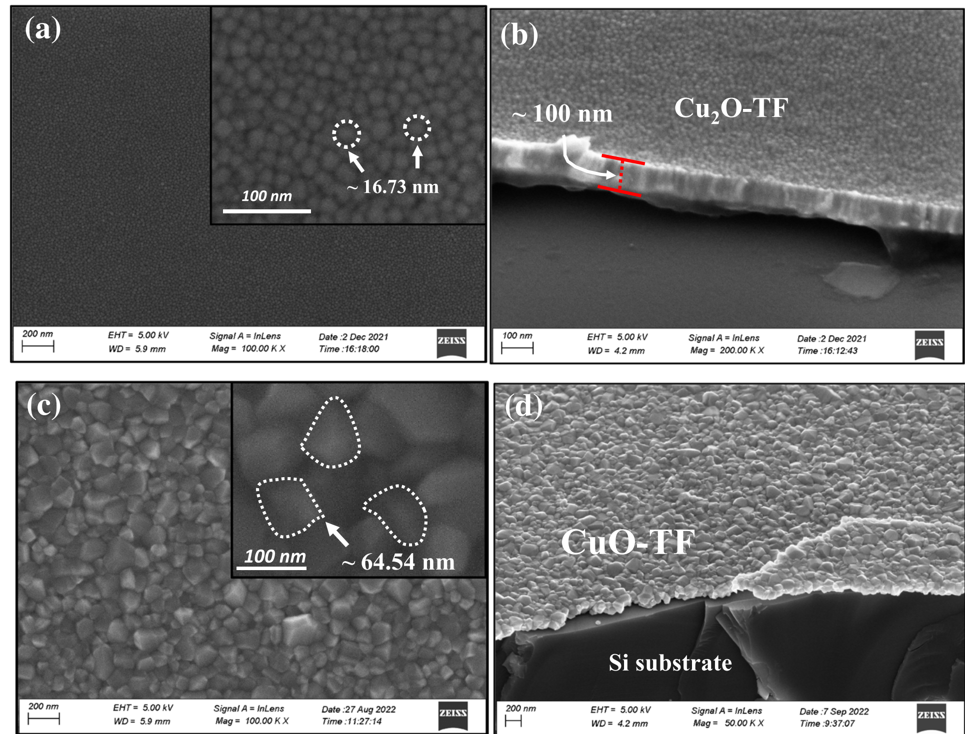

Fig. 4 **a** Top-view SEM image of as-deposited Cu_2O sample, **b** cross-sectional image of as-deposited Cu_2O sample, **c** top-view SEM image of CuO sample after annealing at 600 °C and **d** cross-sectional image of a CuO after annealing at 600 °C

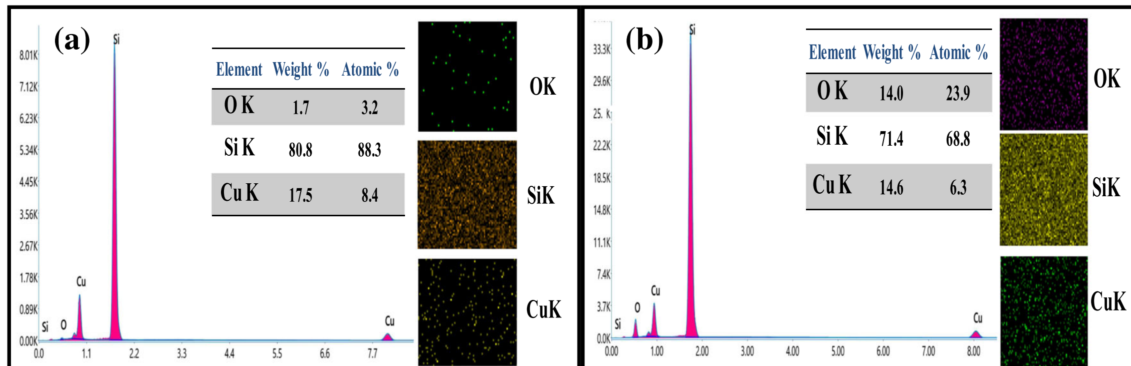

Fig. 5 EDX analysis and chemical mapping showing the presence of copper (Cu), oxygen (O) and silicon (Si) **a** as-deposited sample and **b** sample annealed at 600 °C

method of fabrication and post-deposition annealing method enhance the crystal quality of copper oxide-TF.

3.4 XPS analysis

XPS analysis was performed to investigate the chemical and elemental composition information from the first monolayer surface of the as-deposited Cu_2O-TF and 600 °C annealed CuO-TF samples. The survey spectrum of Cu_2O and CuO films exhibits the direct evidence of Cu and O elements, as shown in Fig. 6a. It can be seen from Fig. 6b that the Cu2p energy level was composed of two main characteristic peaks at ~ 932.54 eV and ~ 952.64 eV, which correspond to $Cu2p^{3/2}$ and $Cu2p^{1/2}$ of the Cu_2O sample, respectively. The spin-orbital splitting, i.e., the peak separation between the two main peaks, was found to be ~ 20 eV, which was in good agreement with the reported value [42]. However, after annealing at 600 °C, new satellite peaks were observed at ~ 940.51 eV, ~ 943.64 eV and ~ 961.56 eV. Therefore, these intense shake-up satellites observed in the Cu2p spectra indicate the formation of CuO on the surface of the film.

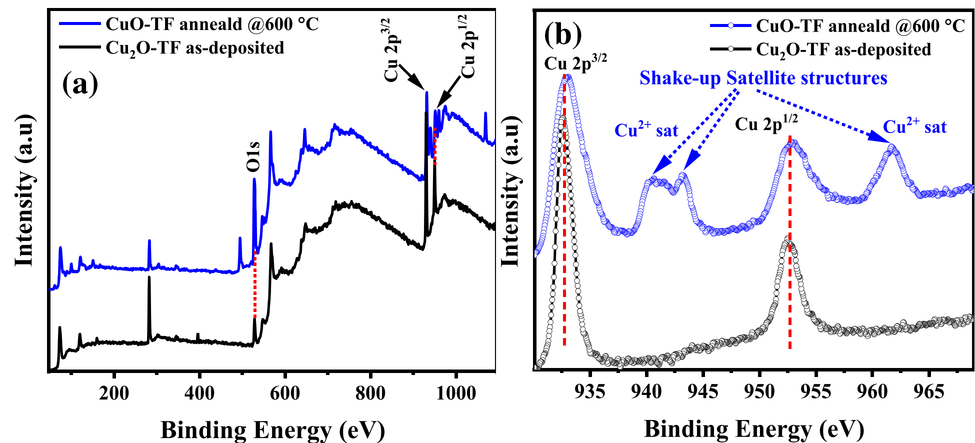

Fig. 6 **a** XPS survey spectrum and **b** Cu 2p XPS core level spectra of as-deposited and annealed copper oxide-TF.

Moreover, this XPS result reveals the presence of the Cu^{+1} phase for the as-deposited sample and the Cu^{+2} phase for the annealed sample, showing the formation of the Cu_2O and CuO phases, which are also observed in the XRD analysis [49]. Therefore, the surface composition evaluated by the XPS strongly indicates the formation of Cu_2O in the as-deposited sample, which changes to the CuO phase after annealing at 600 °C.

4 Conclusion

In this study, copper oxide-TF was successfully deposited using the E-beam evaporation technique on a p-type silicon substrate and then annealed in air for 1 h at various annealing temperatures. The structural and morphological analysis confirms the successful deposition of the copper oxide-TF. The top-view image of the SEM analysis shows the uniform deposition of the copper oxide-TF over the silicon substrate. According to the XRD results, the calculated maximum average crystallite size of the as-deposited Cu_2O-TF sample is found to be ~ 12.98 nm. As the annealing temperature was increased to 600 °C, the calculated average crystallite size gradually increased to ~ 33.54 nm. This increase in grain size can be attributed to the agglomeration of the particles during the recrystallization process. However, with a further increase in the annealing temperature beyond 600 °C, the crystallite size of the CuO-TF decreases, which is due to the breaking of the CuO bond. Moreover, the absorption spectra of the copper oxide-TF show enhanced absorption in the IR region after annealing, which may be due to increased crystallinity, reduced defect density near the band edge and fewer void spaces of the copper oxide film after annealing. The Tauc plot indicates that when the annealing temperature increases to 600 °C the copper oxide film's bandgap gradually reduces from ~ 2.17 to ~ 1.43 eV. This decrease in the bandgap of the copper oxide sample is due to the phase transitioning of Cu_2O to the CuO phase after heat treatment. Therefore, our study demonstrates that annealing is necessary to enhance the quality of copper oxide-TF formed by E-beam evaporation technique so that they can be used in a variety of optoelectronic applications.

Acknowledgements

This work was supported by the Deanship of Scientific Research, Vice Presidency for Graduate Studies and Scientific Research, King Faisal University, Saudi Arabia [Project No. GRANT98]. The authors acknowledge the Department of Electronics and Communication Engineering, Manipur Technical University (MTU), for providing the fabrication facilities (funded by SERB under file no. ECR/2018/000834). The authors would also like to acknowledge NIT, Nagaland, for research facilities. The authors also acknowledge IIT Roorkee, NIT Durgapur for XPS and SEM, as well as NIT Manipur for XRD measurement.

Author contributions

SSS, BS and MWA did the preliminary literature. Fabrication, characterization and analysis of the

result were done by SSS, BS and NKS. Finally, the manuscript was prepared by SSS, BS and NKS. The final manuscript was read and approved by all authors.

Funding

Funding was supported by Deanship of Scientific Research, King Faisal University (Grant number. GRANT98).

Data availability

This article contains the data that supports the findings of the study, which are available from the corresponding author on reasonable request.

Declarations

Conflict of interest There are no conflicts of interest, according to the authors.

References

1. B. Cook, Q. Liu, M. Gong, D. Ewing, M. Casper, A. Stramel, A. Elliot, J. Wu, IEEE Sens. J. **18**, 9542 (2018)
2. A. Younis, D. Chu, S. Li, Sci. Rep. **5**, 13599 (2015)
3. Z. Li, K. Tong, R. Shi, Y. Shen, Y. Zhang, Z. Yao, J. Fan, M. Thwaites, G. Shao, J. Alloys Compd. **695**, 3116 (2017)
4. K. Song, X. Liu, C. Tian, H. Deng, J. Wang, X. Su, Surf. Interfaces **14**, 245 (2019)
5. M. Chang, Q. Li, Z. Jia, W. Zhao, G. Wu, J. Mater. Sci. Technol. **148**, 150 (2023)
6. L. Ren, Y. Wang, X. Zhang, Q. He, G. Wu, Int. J. Miner Metall. Mater. **30**, 504 (2023)
7. A. Umar, A.A. Alshahrani, H. Algarni, R. Kumar, Sens. Actuators B **250**, 24 (2017)
8. B. Shougaijam, S.S. Singh, J. Mater. Sci: Mater. Electron. **32**, 19052 (2021)
9. C. Zhu, A. Osherov, M.J. Panzer, Electrochim. Acta **111**, 771 (2013)
10. O. Diachenko, J. Kováč, O. Dobrozhan, P. Novák, J. Kováč, J. Skriniarova, A. Opanasyuk, Coatings **11**, 1392 (2021)
11. P. Basu, R. Mahesh, S. Harish, S. Joseph, P. Sagayaraj, Appl. Surf. Sci. **449**, 474 (2018)
12. Y. Alajlani, F. Placido, H.O. Chu, R. De Bold, L. Fleming, D. Gibson, Thin Solid Films **642**, 45 (2017)
13. N. Quoc Dung, D. Patil, H. Jung, D. Kim, Biosens. Bioelectron. **42**, 280 (2013)
14. H. Pang, J. Deng, B. Yan, Y. Ma, G. Li, Y. Ai, J. Chen, H. Zheng, J. Du, Int. J. Electrochem. Sci. **7**, 13 (2012)
15. S.M. Pawar, B.S. Pawar, B. Hou, J. Kim, A.T. Aqueel Ahmed, H.S. Chavan, Y. Jo, S. Cho, A.I. Inamdar, J.L. Gunjakar, H. Kim, S. Cha, H. Im, J. Mater. Chem. A **5**, 12747 (2017)
16. K. Mikami, Y. Kido, Y. Akaishi, A. Quitain, T. Kida, Sensors **19**, 211 (2019)
17. S. Barua, G. Das, L. Aidew, A.K. Buragohain, N. Karak, RSC Adv. **3**, 14997 (2013)
18. W. Li, X. Cui, K. Junge, A.-E. Surkus, C. Kreyenschulte, S. Bartling, M. Beller, ACS Catal. **9**, 4302 (2019)
19. S. Zhang, J. Li, X. Jin, G. Wu, Int. J. Miner Metall. Mater. **30**, 428 (2023)
20. J. Lillo-Ramiro, J.M. Guerrero-Villalba, M.L. de Mota-Gonzalez, F.S. A-Tostago, G. Gutiérrez-Heredia, I. Mejía-Silva, A.C. Castillo, Optik **229**, 166238 (2021)
21. D. Chua, S.B. Kim, K. Li, R. Gordon, ACS Appl. Energy Mater. **2**, 7750 (2019)
22. N.M. Rosas-Laverde, A.I. Pruna, J. Cembrero, D. Busquets-Mataix, Coatings **10**, 935 (2020)
23. M. Ozga, J. Kaszewski, A. Seweryn, P. Sybilski, M. Godlewski, B.S. Witkowski, Mater. Sci. Semiconduct. Process. **120**, 105279 (2020)
24. S. Dolai, R. Dey, S. Das, S. Hussain, R. Bhar, A.K. Pal, J. Alloys Compd. **724**, 456 (2017)
25. K.G. Yang, P. Hu, S.X. Wu, L.Z. Ren, M. Yang, W.Q. Zhou, F.M. Yu, Y.J. Wang, M. Meng, G.L. Wang, S.W. Li, Mater. Lett. **166**, 23 (2016)
26. R.D. Prabu, S. Valanarasu, V. Ganesh, M. Shkir, S. AlFaify, A. Kathalingam, S.R. Srikumar, R. Chandramohan, Mater. Sci. Semiconduct. Process. **74**, 129 (2018)
27. C. Abinaya, K. Bethke, V. Andrei, J. Baumann, B. Pollakowski-Herrmann, B. Kanngießer, B. Beckhoff, G.C. Vásquez, J. Mayandi, T.G. Finstad, K. Rademann, RSC Adv. **10**, 29394 (2020)
28. M.I. Hossain, Y. Zakaria, A. Zikri, A. Samara, B. Aissa, F. El-Mellouhi, N.S. Hasan, A. Belaidi, A. Mahmood, S. Mansour, Mater. Technol. **37**, 248 (2022)
29. P. Chiu, Y.-T. Liao, H.-Y. Tsai, D. Chiang, AIP Adv. **8**, 025016 (2018)
30. P.K.K. Kumarasinghe, A. Dissanayake, B.M.K. Pemasiri, B.S. Dassanayake, Mater. Sci. Semiconduct. Process. **58**, 51 (2017)
31. Y. Li, R. Zhang, L. Du, Q. Zhang, W. Wang, Catal. Sci. Technol. **6**, 73 (2016)
32. D. Ozaslan, O. Erken, M. Gunes, C. Gumus, Phys. B: Condens. Matter. **580**, 411922 (2020)

33. M.T.S. Nair, L. Guerrero, O.L. Arenas, P.K. Nair, Appl. Surf. Sci. **150**, 143 (1999)
34. P.V. Raghavendra, J.S. Bhat, N.G. Deshpande, Superlattices Microstruct. **113**, 754 (2018)
35. A.H. Jayatissa, K. Guo, A.C. Jayasuriya, Appl. Surf. Sci. **255**, 9474 (2009)
36. G. Sinha, K. Adhikary, S. Chaudhuri, Opt. Mater. **29**, 718 (2007)
37. Y.M. Abdulraheem, S. Ghoraishi, L. Arockia-Thai, S.K. Zachariah, M. Ghannam, Adv. Mater. Sci. Eng. **2013** 10 (2013). https://doi.org/10.1155/2013/574738
38. A.L. Patterson, Phys. Rev. **56**, 978 (1939)
39. B. Kavitha, M. Nirmala, A. Pavithra, Annealing effect on nickel oxide nanoparticles synthesized by sol-gel method. WSN **52**, 118–129 (2016)
40. A.O. Musa, T. Akomolafe, M.J. Carter, Sol. Energy Mater. Sol. Cells **51**, 305 (1998)
41. S.K. Pandey, S.K. Pandey, V. Awasthi, A. Kumar, U.P. Deshpande, M. Gupta, S. Mukherjee, Bull. Mater. Sci. **37**, 983 (2014)
42. F.A. Akgul, G. Akgul, N. Yildirim, H.E. Unalan, R. Turan, Mater. Chem. Phys. **147**, 987 (2014)
43. A.M. Koshy, A. Sudha, P. Gollapalli, S.K. Yadav, P. Swaminathan, J. Mater. Sci: Mater. Electron. **33**, 13539 (2022)
44. R. Bunea, A.K. Saikumar, K. Sundaram, Mater. Sci. Appl. **12**, 182 (2021)
45. A. Hojabri, F. Hajakbari, N. Soltanpoor, M.S. Hedayati, J. Theor. Appl. Phys. **8**, 132 (2014)
46. P. Chetri, J.C. Dhar, Semicond. Sci. Technol. **35**, 045014 (2020)
47. D. Santos-Cruz, S.A. Mayén-Hernández, F. de Moure-Flores, J. Campos-Álvarez, M. Pal, J. Santos-Cruz, Results Phys. **7**, 4140 (2017)
48. W.-J. Lee, X.-J. Wang, Coatings **11**, 864 (2021)
49. X. Yuan, X. Yan, C. Zhou, J. Wang, D. Wang, H. Jiang, Y. Zhu, X. Tao, X. Cheng, Ceram. Int. **46**, 435 (2020)

Publisher's note Springer Nature remains neutral with regard to jurisdictional claims in published maps and institutional affiliations.

Springer Nature or its licensor (e.g. a society or other partner) holds exclusive rights to this article under a publishing agreement with the author(s) or other rightsholder(s); author self-archiving of the accepted manuscript version of this article is solely governed by the terms of such publishing agreement and applicable law.